energies

MDPI

Article

Vortex-Induced Vibration Characteristics of a PTC Cylinder with a Free Surface Effect

Dahai Zhang [1], Lei Feng [1], Hao Yang [1], Tianjiao Li [1] and Hai Sun [2,3,*]

[1] College of New Energy, China University of Petroleum (East China), Qingdao 266580, China; dhzhang@upc.edu.cn (D.Z.); fengleiww@163.com (L.F.); yh96ao@163.com (H.Y.); tigana0812@163.com (T.L.)
[2] College of Aerospace and Civil Engineering, Harbin Engineering University, Harbin 150001, China
[3] Marine Renewable Energy Laboratory, Department of Naval Architecture & Marine Engineering, University of Michigan, 2600 Draper Road, Ann Arbor, MI 48109-2145, USA
* Correspondence: sunhai2009@gmail.com

Received: 24 September 2019; Accepted: 20 January 2020; Published: 18 February 2020

Abstract: The experimental study of vortex induced vibration needs to be carried out in water tunnel, but in previous associated simulation work, the water tunnel was treated as an infinite flow field in the depth direction with the effect of the free surface neglected. In the paper, the dynamic characteristics and physical mechanisms of a passive turbulence control (PTC) cylinder in a flow field with a free surface is studied, and the combined technique of a volume of fluid (VOF) method and vortex-induced vibration (VIV) was realized. In the range of Reynolds number studied in this paper ($3.5 \times 10^4 \leq Re \leq 7.0 \times 10^4$), the dynamic parameters (lift and drag coefficients), vortex structures, VIV response (amplitude and frequency ratios), and energy harvesting characteristics of a PTC cylinder under different flow conditions were obtained. The study found that: (1) the shear layer was made more unstable behind the cylinder by the free surface, which made it quicker to reach periodic stability, and the asymmetry shortened the initial stage of vibration of the oscillator, which made it easier to produce dynamic control of the motion of the oscillator; (2) the presence of the free surface only affected the positive amplitude ratio, but had almost no effect on the negative amplitude ratio; (3) the frequency ratio in the free surface flow was closer to the experimental data; (4) the presence of the free surface did not affect the detached vortex pattern in the flow around the stationary cylinder, but in the VIV, the lower the free surface height Z, the more vortices that were shed from the moving cylinder.

Keywords: PTC; VIV; free surface; energy harvesting

1. Introduction

The phenomenon of vortex induced vibration (VIV) widely exists in engineering, especially in the fields of oil, port, coastal, and offshore engineering. Experts and scholars at home and abroad have undertaken in-depth and meticulous research on this phenomenon, including Feng [1], Sarpkaya [2], Bearman [3], Williamson [4], Ali [5], and Lian [6].

In most engineering applications, the VIV phenomena are suppressed due to its destructive nature. However, the VIVACE converter (vortex-induced vibration for aquatic energy converter) developed by the Marine Renewable Energy Laboratory (MRELab) of the University of Michigan, uses Flow Induced Vibration (FIV)(including VIV, galloping, and a combination of the two) to convert marine hydrokinetic (MHK) to usable electricity [7–9]. The VIVACE has been in development for more than ten years, both experimentally and numerically [10–12], where several valuable tools, such as PTC (passive turbulence control) and Vck (virtual spring-damping system), are in development to facilitate the FIV experiments.

A free surface exists in many vortex-induced vibration phenomena. On the one hand, in the utilization of tidal energy, the oscillator will be affected by the free surface fluctuations during the rising and ebbing tides. On the other hand, the tubes in a heat exchanger in ocean engineering suffers from the sloshing of a gas–liquid two-phase free surface [13], which causes liquid splashing and reduces the performance of the heat exchanger. Therefore, the existence of a free surface will affect the vortex-induced vibration phenomenon. At present, most experts and scholars have not considered the influence of a free surface on VIV performance. When the oscillator vibrates, the pressure distribution of the oscillator in the flow field with a free surface is different from that without a free surface, and the vortex shedding is also affected. Therefore, it is necessary to consider the influence of a free surface when studying the VIV phenomenon.

Ding et al. [14–16] numerically studied the VIV of one to four rigid circular cylinders in tandem in a high Reynolds number range of 30,000 < Re < 105,000. The simulation results were in good agreement with experimental data, and an oscillatory amplitude of 3.5 diameters was reached in galloping for Re = 105,000. In order to eliminate the influence of a free surface, the computation domain in their simulation was set to 13*D*. Karim et al. [17] used a volume of fluid (VOF) method to simulate the two-phase flow of a NACA0015 hydrofoil moving near the free water surface at different submerged depths. Mansoorzadeh et al. [18] experimentally studied the flow behavior of an underwater vehicle in a water channel and the functions of the drag coefficient and velocity with submerged depth were obtained. Compared with the result of a single-phase case without a free surface effect, the drag coefficient was closer to that of a single phase with the increase of the submerged depth.

Up to now, most of the experimental and simulation studies of vortex-induced vibration of blunt bodies use a uniform, symmetrical single-phase flow field. In the MRELlab laboratory, the circulating water tunnel has a free water surface. In the previous simulations, the researchers simplified the experimental conditions and studied the uniform flow field without considering the influence of the free surface. Therefore, in order to study the vortex-induced vibration of a PTC cylinder more accurately and to find a method of enhancing energy output, the vortex-induced vibration of a PTC cylinder in a non-uniform flow field with a free surface was studied and presented in this paper. The geometric model, physical model, mathematical model, and grid system are presented in Section 2. The simulation results and detailed flow fields are shown in Section 3. Conclusions are drawn at the end.

2. Computational Model

2.1. Geometry and Boundary Conditions

In this study, the computational domain was $30D \times 15D$, as shown in Figure 1. U represents the velocity of the inlet and the velocity magnitude of the entrance was uniform, and the velocity magnitude for air and water was the same. The range of Re based on U and the viscosity of water is $3.5 \times 10^4 \leq Re \leq 7.0 \times 10^4$. The height of the cylinder axis to the free surface was Z ($3.5D < Z < 5.5D$). Considering the effect of the water inflow at the entrance, the distance between the cylinder and the entrance was 10*D*. With the help of a multiphase model using the VOF method, the volume fraction of water for the upper part was set to 0, and the lower part was set to 1 with the gravity applied along the Y-axis negative direction. The pressure outlet boundary condition and no slip wall boundary condition for the top and bottom boundary were used in the present simulation.

It should be noted that if taking the X-axis as the symmetric axis, the PTC cylinder had a symmetric geometry, while for the flow field with a free surface, because of the different flow media, the upper half and the lower half of the cylinder will experience different flow pressures. The flow field had an asymmetric incoming flow, and with the decreasing of Z, the asymmetry became more pronounced. On the contrary, the flow of a single phase with uniform velocity could be taken as a symmetric incoming flow.

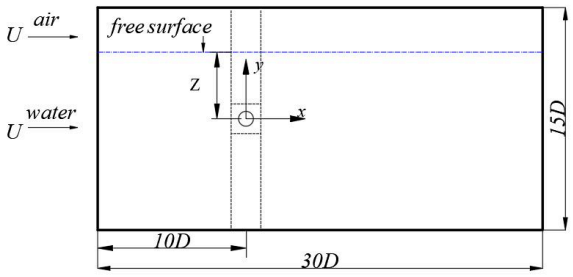

Figure 1. Computational domain.

Based on the MRElab experimental device [19], the influence of the incoming flow with a free surface on the flow characteristics of a circular cylinder was studied for this paper. The diameter of the PTC cylinder was D (D = 0.0889 m), as shown in Figure 2. The placement position of the rough band was α_{PTC} at 20°, the coverage angle β was 16°, and the rough band was symmetrically distributed on both sides of the cylinder; for more details of the rough belt, please refer to References [10,11,19]. In order to quantitatively describe the force on the surface of a cylinder, a polar coordinate system with the center of the cylinder as the origin and the front stagnation point as the starting point was established for the cross-section of the cylinder. Any point on the surface of the cylinder was described using its polar angle θ, just as shown in Figure 2. If the clockwise direction is positive, the front stagnation point of the cylinder was θ = 0° and the rear stagnation point was θ = 180°.

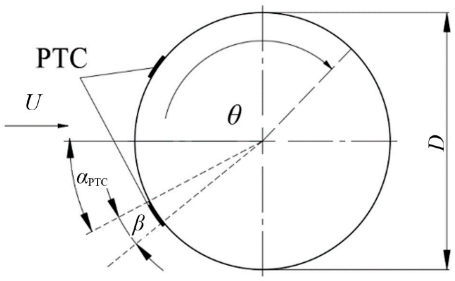

Figure 2. Details of the roughness strip.

2.2. Mesh

Two-dimensional, structured, computational grids were generated with the multi-block generation technique to make the ununiformed grid, which is shown in Figure 3a; this could guarantee a high enough calculation precision with less computational time, and the grids around the cylinder were refined, as shown in Figure 3b. The grid density near the surface was crucial to the calculation of the surface pressure of the oscillator. For the PTC step, we adopted the two-layer mesh with a corresponding maximum y^+ equal to 16. For more details of the grid, refer to Zhang et al. [20]. The grid independence of the model was verified. When the Reynolds number was 3.5×10^4, three different grids of the PTC cylinder were tested. As shown in Table 1, the maximum lift coefficient and the root mean square value of the drag coefficient of the stationary cylinder were compared under three different grids. Considering the calculation accuracy and computer calculation costs, this study used a medium density grid for the calculations.

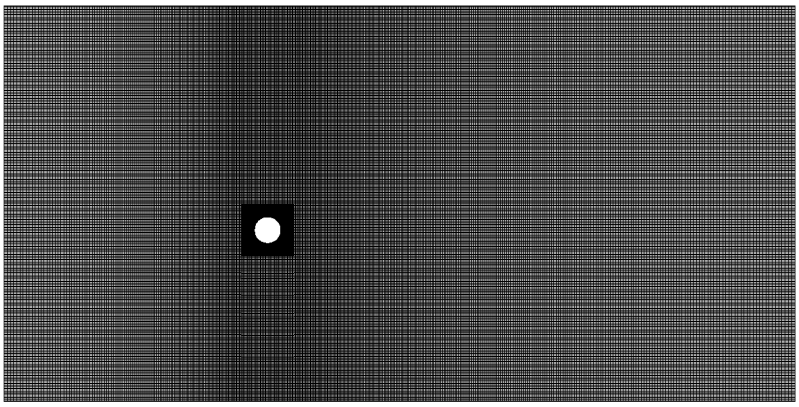

(a) Non-uniform grid system

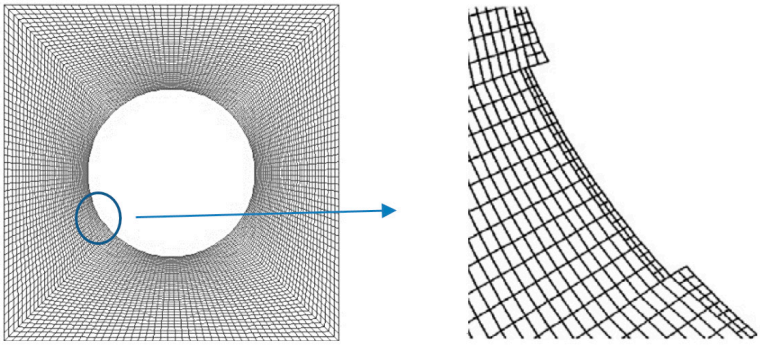

(b) Grid in the vicinity of the cylinder

Figure 3. Grid system.

Table 1. Grid independent verification (Re = 35,000).

Grid (Central Square: Circumferential × Radial)	C_L, max	C_D, rms
Coarse (120 × 30)	1.825	1.577
Medium (180 × 45)	1.836	1.548
Fine (240 × 60)	1.837	1.549

2.3. Mathematical Model

The transient, viscous fluid solutions were obtained using a numerical approximation of the incompressible 2D-URANS equations with the one-equation Spalart–Allmaras turbulence model. The mathematical formulations can be described as follows [21]:

$$\frac{\partial u_i}{\partial x_i} = 0, \tag{1}$$

$$\frac{\partial u_i}{\partial t} + u_j \frac{\partial u_i}{\partial x_j} = -\frac{1}{\rho}\frac{\partial p}{\partial x_i} + \frac{\partial}{\partial x_j}(2\nu S_{ij} - \overline{u_j' u_i'}), \tag{2}$$

$$S_{ij} = \frac{1}{2}\left(\frac{\partial u_i}{\partial x_j} + \frac{\partial u_j}{\partial x_i}\right), \tag{3}$$

where ν is the molecular kinematic viscosity, ρ is the fluid density, u_i is the mean flow velocity vector, and S_{ij} is the mean strain-rate tensor.

The quantity $\tau_{ij} = -\overline{u'_i u'_j}$ is known as the Reynolds stress. A common method employs the Boussinesq approximation to relate the Reynolds stress to the mean strain-rate tensor in the Spalart–Allmaras model using:

$$\tau_{ij} = 2\mu_t S_{ij}, \tag{4}$$

where μ_t is the kinetic eddy viscosity, with the corresponding defining equation is as follows:

$$\mu_t = \rho\widetilde{\upsilon} f_{\upsilon 1},\ f_{\upsilon 1} = \frac{x^3}{x^3 + {c_{\upsilon 1}}^3},\ x = \frac{\widetilde{\upsilon}}{\upsilon}, \tag{5}$$

where $\widetilde{\upsilon}$ is the intermediate working variable of the turbulence model that obeys the following transport equation [21]:

$$\frac{\partial \widetilde{\upsilon}}{\partial t} + u_j \frac{\partial \widetilde{\upsilon}}{\partial x_j} = c_{b1}\widetilde{S}\widetilde{\upsilon} - c_{w1} f_w \left(\frac{\widetilde{\upsilon}}{d}\right)^2 + \frac{1}{\sigma}\left\{\frac{\partial}{\partial x_i}\left[(\upsilon + \widetilde{\upsilon})\frac{\partial \widetilde{\upsilon}}{\partial x_j}\right] + c_{b2}\frac{\partial \widetilde{\upsilon}}{\partial x_j}\frac{\partial \widetilde{\upsilon}}{\partial x_j}\right\}. \tag{6}$$

The tracking of the interface(s) between the phases is accomplished using the solution of a continuity equation for the volume fraction of one (or more) of the phases. For the qth phase, this equation has the following form [22]:

$$\frac{1}{\rho_q}\left[\frac{\partial}{\partial t}\left(\alpha_q \rho_q\right)\right] + \nabla\left(\alpha_q \rho_q \vec{v_q}\right) = S_{\alpha_q} + \sum_{p=1}^{n}\left(\dot{m}_{pq} - \dot{m}_{qp}\right),$$

where $\dot{m}_{qp}$ is the mass transfer from phase q to phase p and $\dot{m}_{pq}$ is the mass transfer from phase p to phase q.

In order to get the displacement of the oscillator, the fluid–solid coupling technique was used to capture the vibration information of the oscillator, and the one-degree of freedom equation of motion of the oscillator can be given as:

$$m_{osc}\ddot{y} + C_{total}\dot{y} + Ky = F, \tag{7}$$

where m_{osc} is the total oscillating mass of the cylinder and attachments including one-third of the spring mass, and F is the total lift force that can be achieved by integrating the surface pressure of the PTC cylinder. In the present study, for the consistency with the experiment [19], the constant damping and spring stiffness was used: ζ_{total} = 0.14 and K = 600. The relationship of ζ_{total} and C_{total} is shown as the following equation:

$$\zeta_{total} = \frac{C_{total}}{2\sqrt{m_{osc}K}}. \tag{8}$$

The acceleration term $\ddot{y}$ can be solved using Equation (7), then its velocity and displacement can be calculated using:

$$y_{t+1} = y_t + U_{t+1} \cdot \Delta t, \tag{9}$$

$$U_{t+1} = U_t + a_{t+1} \cdot \Delta t. \tag{10}$$

The cylinder was assumed to be at the origin (y = 0) and stable at t = 0. The initial conditions in mathematical terms were:

$$y_0 = U_0 = 0. \tag{11}$$

The displacement of the cylinder in VIV could therefore be written as:

$$y_{t+1} = y_t + U_t \cdot \Delta t + a_{t+1} \cdot (\Delta t)^2. \tag{12}$$

Returning to Equation (7) and rewriting the numerical displacement equation gives:

$$y_{t+1} = y_t + U_t \cdot \Delta t + \left(\frac{F_{t+1} - cU_t - ky_t}{m}\right) \cdot (\Delta t)^2. \tag{13}$$

Equation (13) gives the displacement of the cylinder at each time step. The force applied by the fluid will commence the oscillatory movement of the cylinder.

The commercial software package FLUENT (version 19.2), from ANSYS, Inc., USA, combined with User Defined Function to solve the oscillator equation, was used to numerically solve the unsteady Reynolds-averaged Navier–Stokes equations in this study, and the time step size was 0.001 s. The pressure-based solver and the SIMPLE algorithm was used to couple the pressure and velocity. The QUICK scheme was used for spatial discretization of the convective terms. The convergence criteria for the continuum equation was 1×10^{-3}, while for other equations, it was 1×10^{-5}.

The physical model in this paper can be seen as a simplification of VIVACE. The theoretical fluid power (P_{fluid}), the actual output power (P_{VIVACE}), and the conversion efficiency (η) are also important parameters to measure the performance of VIVACE. According to the hydrodynamic pressure formula, the theoretical power of a flow-induced vibration of a cylinder is obtained as follows:

$$P_T = \frac{1}{2}\rho U^2, \tag{14}$$

$$F_x = \frac{1}{2}\rho U^2 (2A_{\max} + D)L, \tag{15}$$

$$P_{fluuid} = F_x U = \frac{1}{2}\rho U^3 (2A_{\max} + D)L. \tag{16}$$

The actual output power (P_{VIVACE}) of the VIVACE system is calculated using the work done by the water force on the cylinder within a period:

$$P_{VIVACE} = \frac{W_{VIVACE}}{T_{osc}} = \frac{1}{T_{osc}} \int_0^{T_{osc}} F_{fluid} \dot{y} dt, \tag{17}$$

$$P_{VIVACE} = \frac{W_{VIVACE}}{T_{osc}} = \frac{1}{T_{osc}} \int_0^{T_{osc}} (m\ddot{y} + c\dot{y} + ky)\dot{y} dt. \tag{18}$$

According to the simplified model, the vibration displacement curve of a cylinder is known to be a sinusoidal curve, and its displacement equation and velocity equation are listed respectively:

$$y = A_{\max} \sin(\omega_{osc} t), \tag{19}$$

$$\dot{y} = A_{\max} \omega_{osc} \cos(\omega_{osc} t). \tag{20}$$

Therefore:

$$P_{VIVACE} = 8\pi^3 m C_{system} f_{n,water} {A_{max}}^2 {f_{osc}}^2, \tag{21}$$

where, the damping C_{system} is calculated using Equation (8) with the damping ratio ζ_{system} chosen to be 0.02. $f_{n,water}$ is the natural frequency in water of the oscillator, and f_{osc} is the vibration frequency of the oscillator.

Finally, the conversion efficiency of VIVACE system was calculated using a Betz limit B of 59.26% [19]:

$$\eta = \frac{P_{VIVACE}}{P_{fluid} \times Betz\text{limit}} = \frac{16\pi^3 C_{system} f_{n,water} {A_{max}}^2 {f_{osc}}^2}{\rho U^3 (2A_{\max} + D)L \times B}. \tag{22}$$

3. Results and Discussion

3.1. Hydrodynamic Characteristics

In this part, the hydrodynamic characteristics, including the lift, drag, and surface pressure coefficients, of the flow around the stationary PTC cylinder and flow induced vibration are introduced.

3.1.1. Lift and Drag Coefficient

(a) Stationary Cylinder

Figure 4 shows the lift coefficient time history curve of the PTC cylinder at different free surface heights when Re = 3.5×10^4. Compared with the result of a symmetric flow field without a free surface, the existence of a free surface could shorten the convergence time to reach periodic stability for the PTC cylinder calculation; the lower the height of the free surface, the shorter the stable convergence time. Therefore, we could draw the conclusion that asymmetry was more likely to cause instability in the shear layer behind the cylinder, and then arouse a Kelvin–Helmholtz instability, which was more likely to cause the formation of a Kármán vortex street. The shedding of the small random vortices promoted the development of shedding vortices until the periodic steady state. The smaller the free surface height, the more obvious the asymmetry, and the earlier the Kármán vortex street was formed; correspondingly, the vortex development reached periodic stability faster. This phenomenon was further confirmed by Figure 5, which shows the drag coefficient time history curve of the PTC cylinder at different free surface heights when Re = 3.5×10^4. It can be seen from the graph that the drag coefficient increased slightly with the decrease of the free surface height. At the same time, it can also be seen that, consistent with the variation trend of lift coefficient, the smaller the height of the free surface, the earlier the formation of a Kármán vortex street, and therefore, the quicker the drag coefficient reached the periodic steady state.

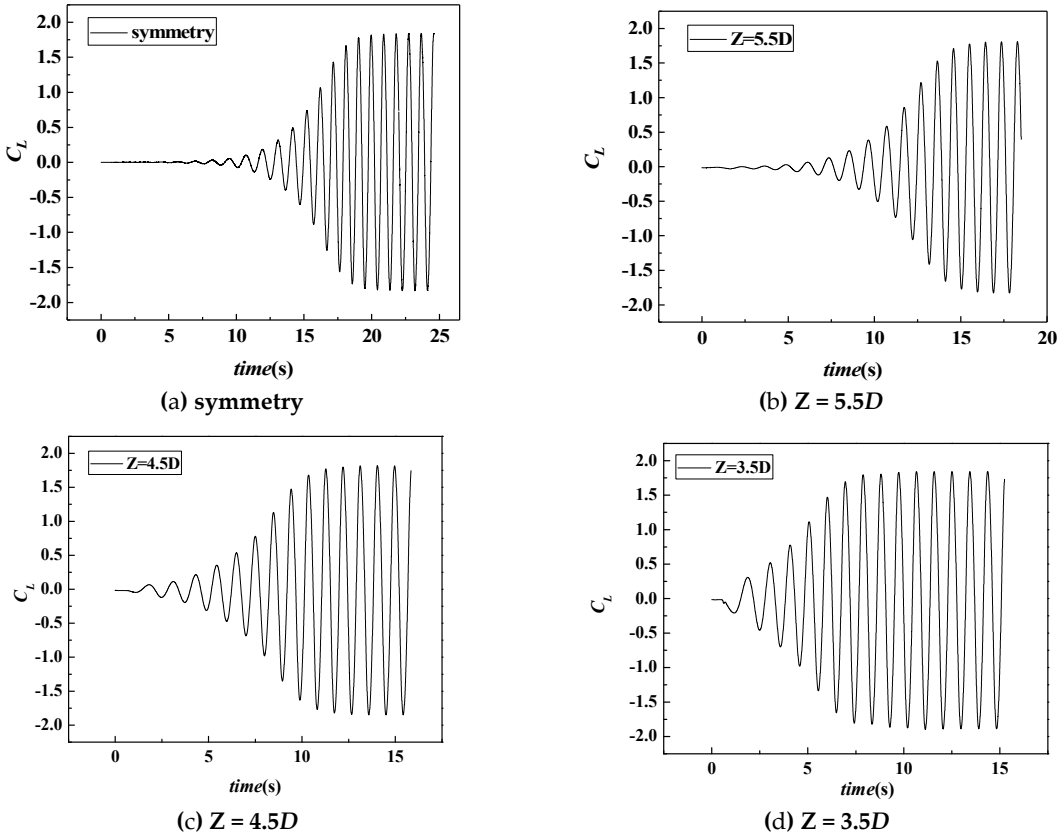

Figure 4. Time history of C_L of the stationary cylinder at different free surface heights Z ($Re = 3.5 \times 10^4$).

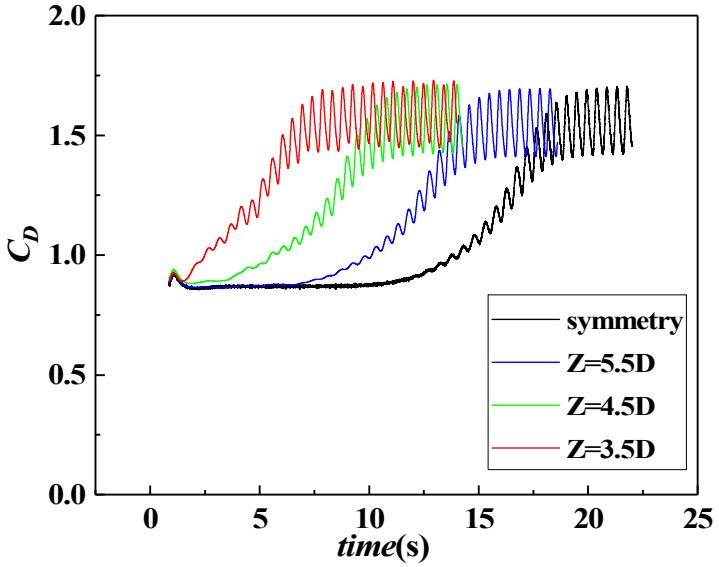

Figure 5. Time history of C_D of the stationary cylinder at different free surface heights Z ($Re = 3.5 \times 10^4$).

(b) Flow-Induced Vibration

Figure 6 shows the lift coefficient time history curve for the flow-induced vibration of the PTC cylinder at different free surface heights when Re = 3.5×10^4. It can be seen from the figure that compared with the uniform incoming flow in a symmetric flow field, the asymmetry of the free surface shortened the starting time of the cylindrical oscillator, thus shortening the response time of the oscillator to the incoming flow, which allows for easier dynamic control of the motion of the oscillator through the change of the flow field in practice. Compared with the flow field around the stationary cylinder, we found that the lift coefficient curve of the oscillator fluctuated sharply during the motion. This can be explained by the fact that unlike a zero attack angle in a stationary state, the reciprocating motion of the PTC cylinder made the actual attack angle of the incoming flow change continually, combined with the effect of the multiple vortex shedding, which resulted in the constant change of the surface pressure, and further lifted the cylinder during the motion cycle. On the other hand, because the motion of the cylinder caused the fluctuation of the free surface, this produced a continuously changing force on the cylinder.

Figure 7 shows the drag coefficient time history curve for the flow-induced vibration of the PTC cylinder at different free surface heights when $Re = 3.5 \times 10^4$. It can be seen that compared with the flow field around the stationary cylinder, the reciprocating motion of a PTC cylinder made the surface pressure of the oscillator change randomly, which led to irregular fluctuations of the drag coefficient. At the same time, we found that the change of the drag coefficient was more irregular compared with that of the lift coefficient, which could be attributed to the fact that in a vibration period, the fluctuation frequency of the drag coefficient was twice that of the lift coefficient, which has been proven by predecessors [2,4].

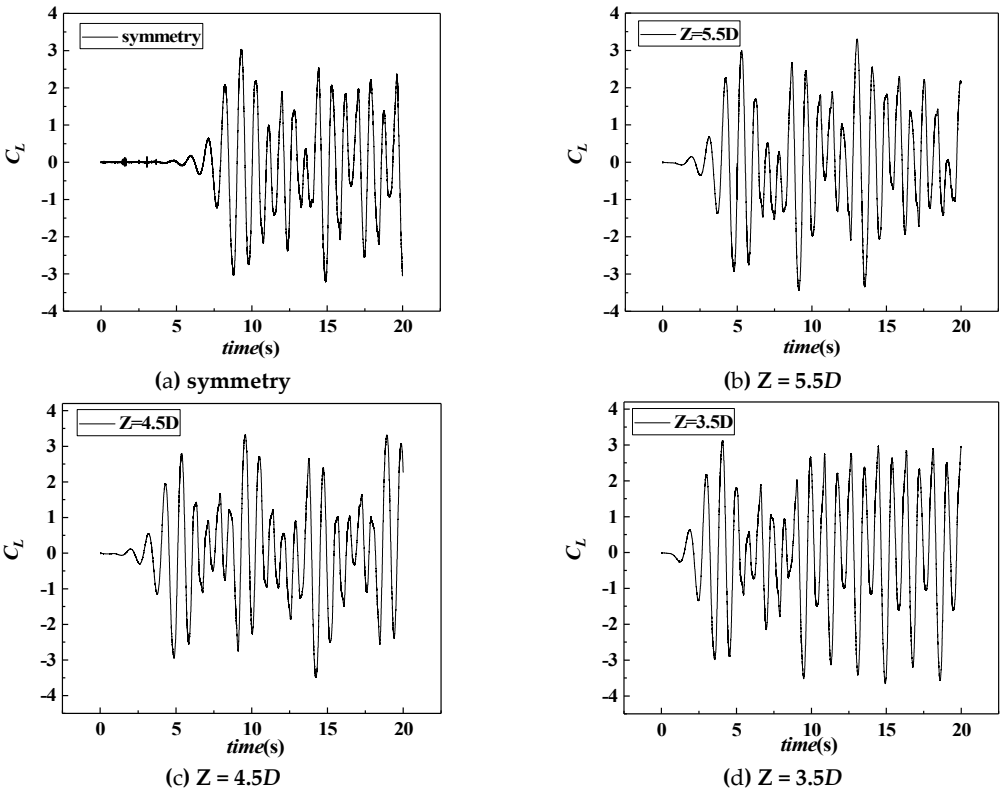

Figure 6. Time history of C_L of the passive turbulence control (PTC) cylinder flow-induced vibration for different Zs (Re = 3.5×10^4).

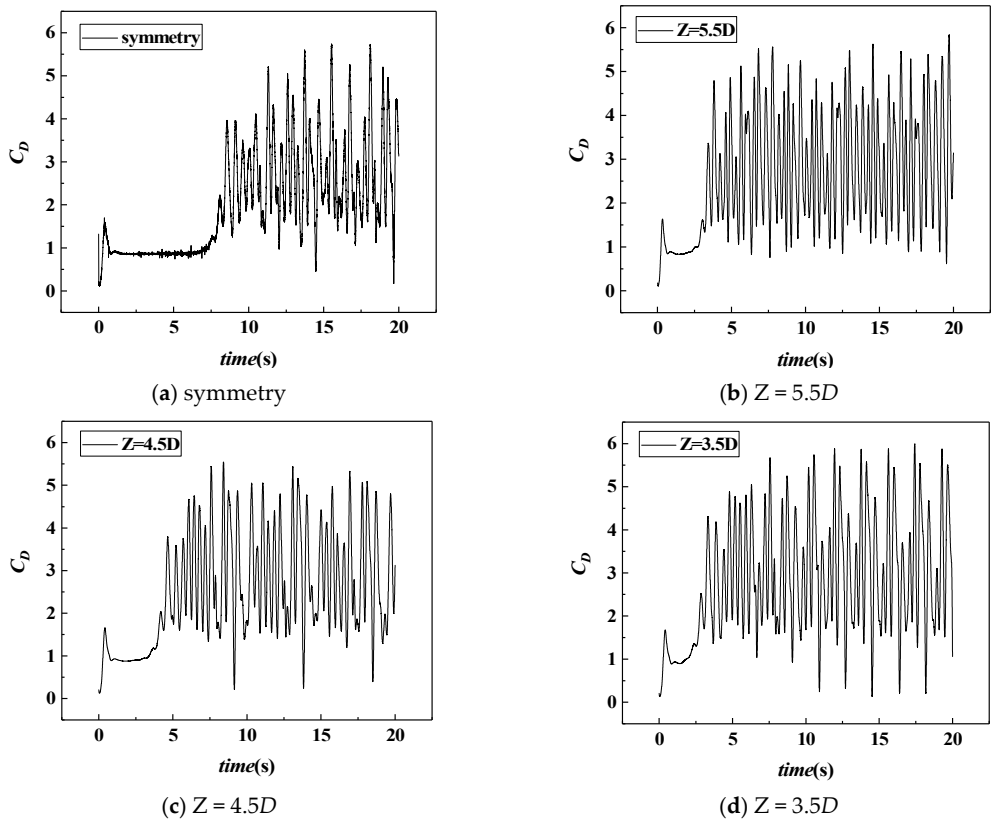

Figure 7. Time history of C_D of the PTC cylinder flow-induced vibration for different Zs ($Re = 3.5 \times 10^4$).

3.1.2. Surface Pressure Coefficient

(a) Stationary Cylinder

In order to show more intuitively the relationship between the surface pressure of a cylinder and its polar angle, the polar angles on the upper and lower surfaces of a cylinder were defined as follows: For the upper surface of a cylinder, the clockwise direction along A→C→B (the solid point in Figure 8) was defined as positive; for the lower surface of a cylinder, the counter-clockwise direction along A→D→B (the hollow point in Figure 8) was defined as positive. The area surrounded by the solid and hollow points represented the pressure difference of the cylinder. The front stagnation point A was equal to 0°, the rear stagnation point B was equal to 180°, C was the highest point on the upper surface of the cylinder, D was the lowest point on the lower surface of the cylinder, S was the separation point on the upper surface, while S′ indicated the separation point on the lower surface.

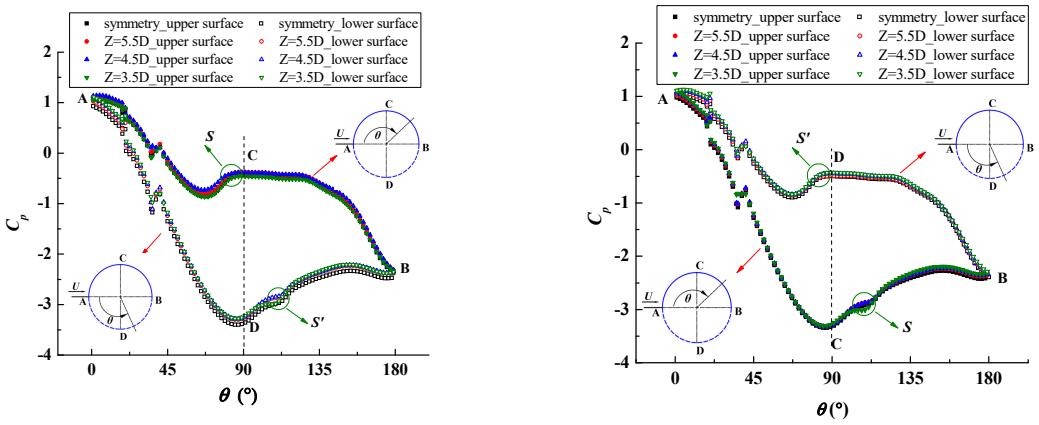

(**a**) Highest position (**b**) Lowest position

Figure 8. The C_p of stationary PTC cylinder varied with the free surface heights Z ($Re = 3.5 \times 10^4$).

As shown in Figure 8, the pressure coefficient C_p on the surface of the PTC cylinder in the free surface flow field varied negligibly relative to the free surface height when $Re = 3.5 \times 10^4$. In the figure, the highest position means the position of the highest point in the lift coefficient curve when the vortex was released from the upper side of the cylinder, and the lowest position means the position of the lowest point in the lift coefficient curve when the vortex was released from the lower side of the cylinder. Regarding the flow around the stationary cylinder, for the range of parameters studied for this paper, the free surface height had little effect on the distribution of pressure coefficient on the surface of the PTC cylinder.

The flow velocity and pressure are closely related. Just as shown in Figure 9, when the free surface height Z = 5.5*D*, the pressure coefficient on the cylinder surface varied with the Reynolds number. It can be seen from the two graphs that the separation points S on the upper surface and S′ on the lower surface of the PTC cylinder developed backward with the increase of the flow velocity, which could be attributed to the fact that the turbulence intensity increased with the increase of the Reynolds number, and stronger turbulence delayed the boundary layer separation. It can also be found from the two graphs that the pressure difference between the upper and lower surfaces of the cylinder decreased with the increase of the Reynolds number, which corresponds to the trend that the lift coefficient decreases with the increase of Reynolds number, as found in the literature [23]. At the same time, it can be seen from the graphs that the pressure coefficients at the front stagnation point A in the free surface flow were all greater than 1. This was because the wave disturbance of the free surface influenced the velocity distribution of the flow field, which made the actual flow velocity larger and the local static pressure smaller. According to the equation for C_p, the pressure coefficient obtained will be larger than 1. Due to the existence of the free surface, the upper part of the PTC cylinder suffered a greater

influence than that of the lower surface, and the C_p of point A in the lowest position was slightly less than that in the highest position.

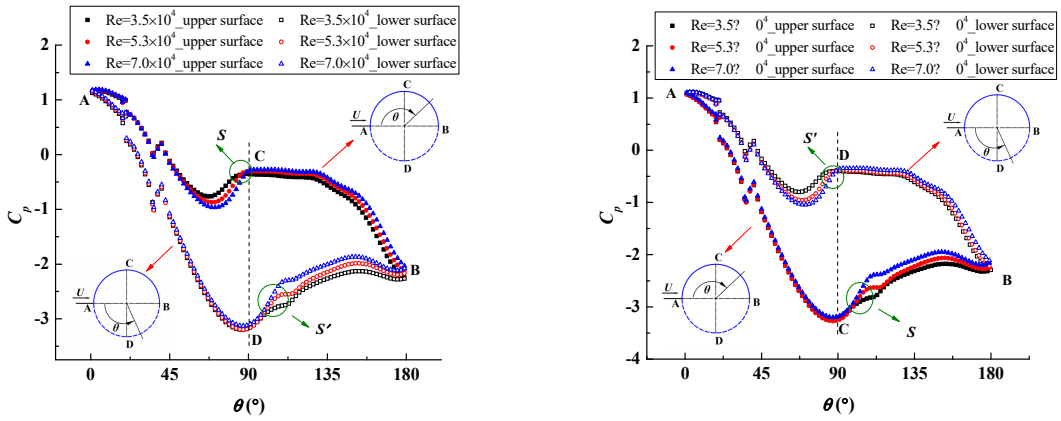

(**a**) Highest position (**b**) Lowest position

Figure 9. The C_p of the stationary PTC cylinder varied with the Reynolds number (Z = 5.5*D*).

(b) Flow-Induced Vibration

In flow-induced vibration, because the cylinder moves up and down, the highest position is redefined as the position of the highest point in the amplitude–time curve, and the lowest position is redefined as the position of the lowest point in the amplitude–time curve. Figures 10 and 11 show the distribution of pressure coefficient C_p of the surface of the PTC cylinder undergoing flow-induced vibration, and C_p varies with Z and Re. It was found that compared with the performance of the flow around the stationary cylinder, the distribution of C_p in the flow-induced vibration showed a dramatic difference. The pressure coefficients of the upper and lower surfaces of the cylinder in the flow-induced vibration intersected, and the pressure distribution in the front half of the cylinder was quite opposite to that of the stationary cylinder. This could be attributed to the fact that the cylinder oscillated in the flow-induced vibration, the attack angle of the incoming flow was not a constant value, and the actual flow direction mainly affected the front surface of the cylinder. In turbulent flow, the vortex shedding separation point of the cylinder occurred on the back of the cylinder, and in laminar flow, the separation point was on the front of the cylinder. Therefore, in the Re range studied for this paper, the intersection point of the pressure coefficient curve of the upper and lower surfaces of the cylinder was behind 90 degrees.

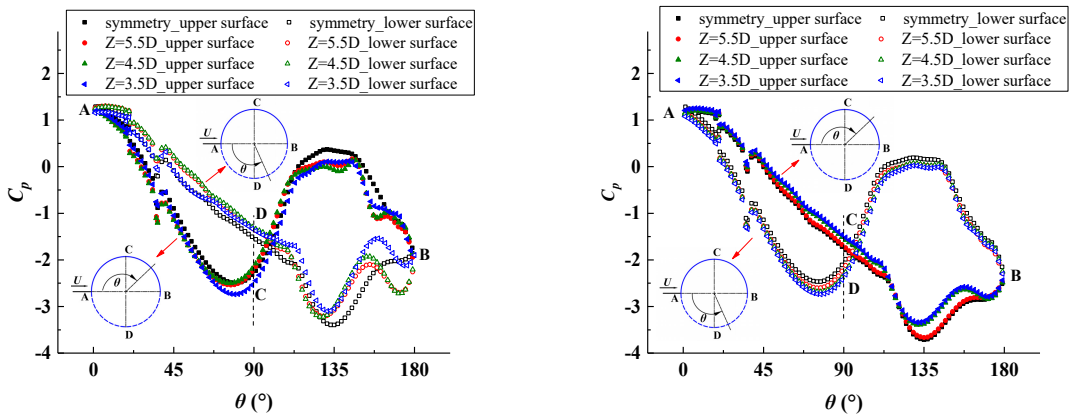

(**a**) Highest position (**b**) Lowest position

Figure 10. The C_p of PTC cylinder in flow induced vibration varies with Z ($Re = 5.3 \times 10^4$).

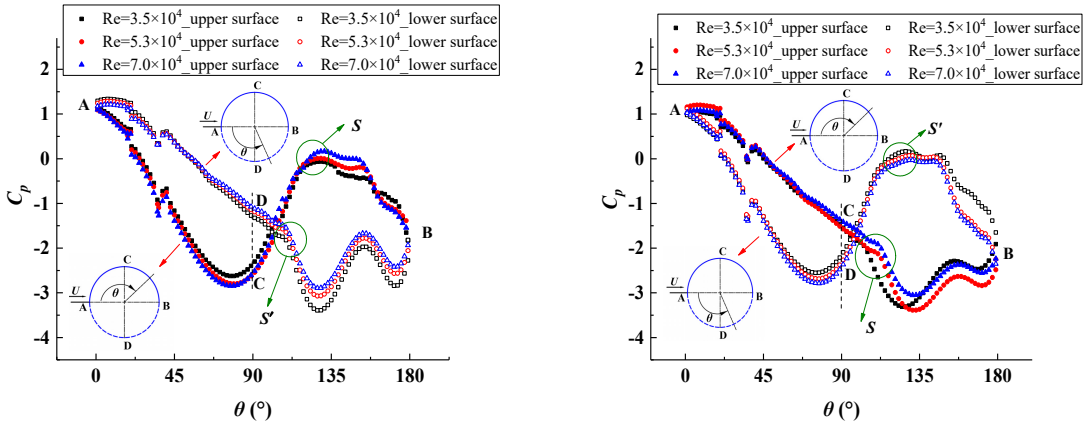

(**a**) Highest position (**b**) Lowest position

Figure 11. The C_p of the PTC cylinder in the flow-induced vibration varied with *Re* (Z = 5.5*D*).

Meanwhile, the separation points of both the upper and lower surfaces of the cylinder moved backwards. This could also be explained by the fact that the actual flow direction for the cylinder changed continuously, and the corresponding pressure distribution of the cylinder surface varied over the oscillating period, which caused the change of the adverse pressure gradient on the back surface of the cylinder.

As shown in Figure 10, compared with the result of the free surface flow, for the front surface of the cylinder, the pressure difference between the upper and lower surfaces in the symmetrical flow field was small, while for the rear of the cylinder, the pressure difference between the upper and lower surfaces in the symmetrical flow field was large. On the whole, the free surface had little effect on the pressure difference between the upper and lower surfaces of the cylinder, and the pressure coefficient on the upper surface of the cylinder varied more than that on the lower surface at different free surface heights, which indicated that the existence of the free surface had a greater impact on the upper surface of the cylinder than on the lower surface.

As shown in Figure 11, the surface pressure coefficients for flow-induced vibration of the PTC cylinder varied with Reynolds number (*Re*) for a constant free surface height Z = 5.5*D*. With the increase of the Reynolds number, the turbulence intensity increased and the separation points S on the upper surface and S′ on the lower surface of the cylinder moved backward, which was the same as that for flow around the stationary cylinder. We also found from the figure that with the increase of the Reynolds number, the pressure coefficient of the front half of the cylinder varied regularly. The greater the Reynolds number, the greater the pressure difference between the upper and lower surfaces, and the greater the lift force on the cylinder. This regularity is consistent with the previous research results [19,21]. Meanwhile, for the rear of the cylinder, due to the influence of shedding vortices, the distribution of the pressure coefficients became somewhat disorderly.

Comparing the two figures of the highest and lowest positions, it was found that the distribution of the pressure coefficients in the two graphs was quite opposite. The downward hydrodynamic force was produced at the highest position, and the upward hydrodynamic force was produced at the lowest position, and the alternating force acted on the cylinder, which made the cylinder accomplish the upward and downward reciprocating motion in the flow-induced vibration.

3.2. Vortex Structure

(a) Stationary Cylinder

When VIV occurs, vortices may shed in the tail of the bluff body. Several basic vortex shedding patterns were defined by Williamson and other researchers [2,4]. “P” means vortex pairs with opposite directions, “S” means a single vortex, and “T” means a triple-vortex wake mode.

As shown in Figure 12, the wake pattern of flow around the stationary PTC cylinder at different Reynolds numbers and free surface heights (Z) is presented. It can be seen from the graph that the vortex pattern of the static PTC cylinder in the free surface flow field were in 2S mode. For the same Reynolds number, taking the Reynolds number Re = 3.5×10^4 as an example, the pattern of the vortex shedding behind the cylinder was the same as that without the free surface. The vortex shedding normally formed the Kármán Vortex Street, and the free surface fluctuated under the influence of the shedding vortex. With the decrease of the Z value, the free surface was clearly affected by the shedding vortex, while the shedding vortex formed behind the cylinder was basically unchanged. At the same free surface height, such as Z = 4.5*D*, with the increase of Reynolds number *Re*, the shedding vortices of the PTC cylinder became gradually larger, which indicated that the ability for releasing vortices was gradually strengthened by the increasing flow velocity. The free surface fluctuated violently with the increase of the Reynolds number, which was due to the larger energy of the shedding vortex at higher Reynolds numbers, which promoted the fluctuation of the free surface.

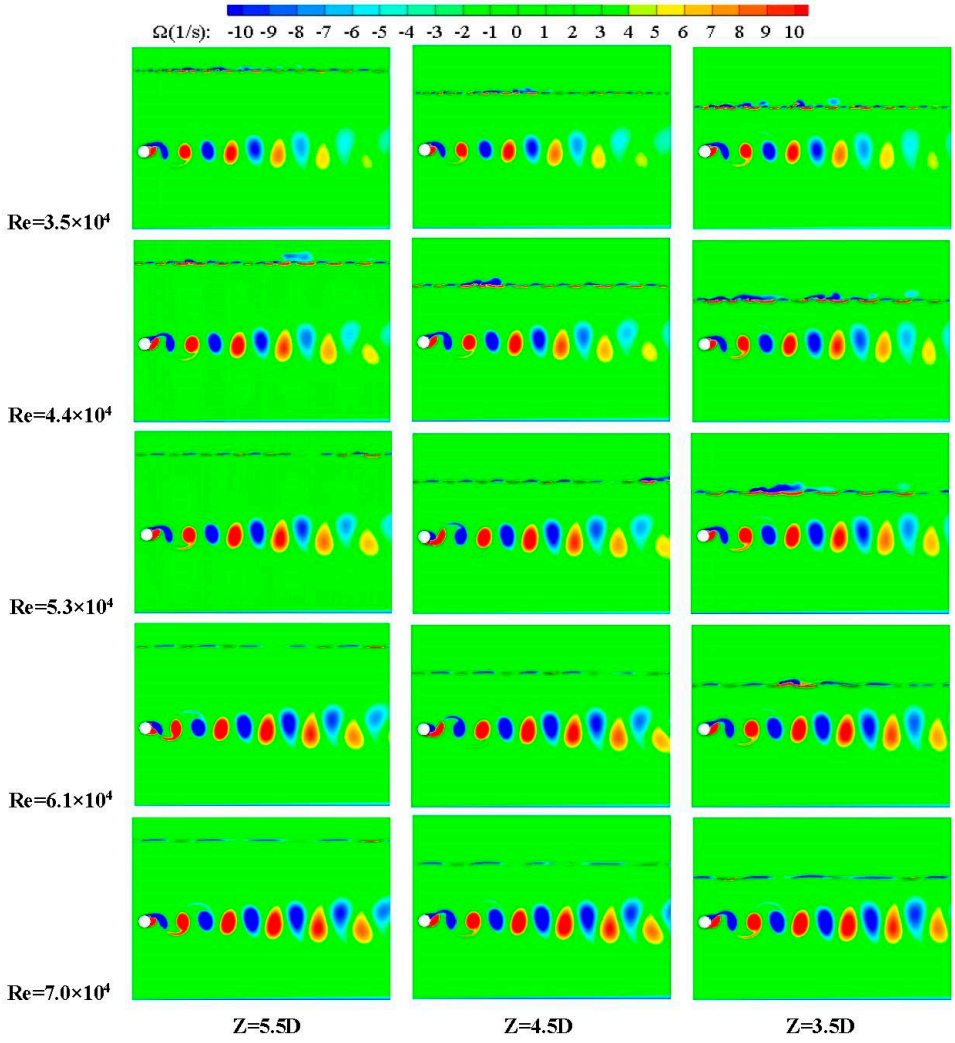

Figure 12. The vortex structure of the stationary PTC cylinder in the free surface flow.

(b) Flow-Induced Vibration

As shown in Figure 13, the wake pattern of the PTC cylinder in a flow-induced vibration at the highest amplitude position in a free surface flow field is presented. When *Re* = 3.5×10^4, the shedding vortex was in 2S mode. When *Re* = 4.4×10^4, the shedding vortex in the free surface flow field showed a 2QP (quasi-pair) mode, which was different from the 2S mode in a symmetric flow field, and the

strength of the vortex increased with the decrease of the free surface height. When $Re = 5.3 \times 10^4$, the wake vortices formed a 2QP structure, which was the same as that in the symmetrical flow field, and the strength of vortices also increased with the decrease of the free surface height. When $Re = 6.1 \times 10^4$ and Z = 5.5*D*, the wake vortices were QP + P, which was the same as that in the symmetrical flow field, while when Z = 3.5*D*, the wake vortices were in 2P mode. When $Re = 7.0 \times 10^4$, the wake vortices were 2P when Z = 5.5*D* and QT (quasi-triple) + T when Z = 3.5*D*.

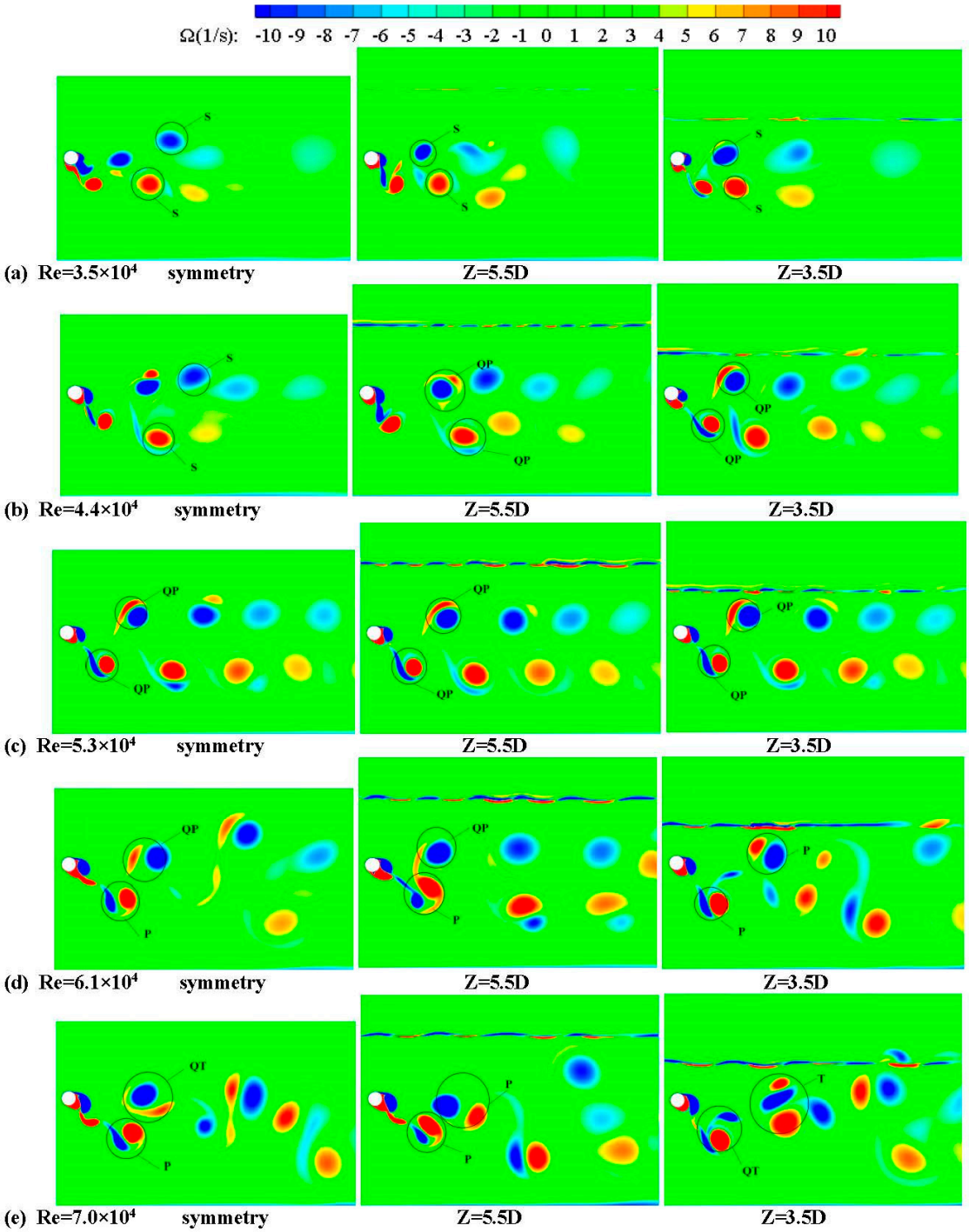

Figure 13. The vortex structure of the flow-induced vibration of the PTC cylinder in the free surface flow.

Within the range of parameters studied, the amount of vortex shedding increased with the increase of the Reynolds number at the same free surface height (Z), and the corresponding wake mode transited

from 2S to 2QP, then to 2P mode, and finally to QT + T mode. At the same Reynolds number, with the decrease of the free surface height, the wake mode was easier to change from single mode to multi-pair mode.

3.3. VIV Response

3.3.1. Amplitude and Frequency

In the asymmetric flow field with the free surface flow, there are three kinds of amplitude. One is the positive amplitude (upward amplitude when the cylinder at the highest position, named $A_{positive}$). Two is the negative amplitude (downward amplitude when the cylinder at the lowest position, named $A_{negative}$). The last one is the average amplitude (named $A_{average}$), which is the arithmetic mean value of $A_{positive}$ and $A_{negative}$ [20].

As shown in Figure 14a, the value of the positive and negative amplitude ratios of the flow-induced vibration of the PTC cylinder varied with Reynolds number in the free surface flow field. It can be seen from the graph that with the increase of the Reynolds number, the positive amplitude of the free surface flow fluctuated compared with the value of the symmetrical flow field, while the negative amplitude ratio of the free surface flow field was almost the same as that of the symmetrical flow field, indicating that the existence of the free surface had an effect on the highest position of the cylinder motion, but almost no effect on the lowest position. In Figure 14b, the average amplitude ratio varied with the Reynolds number in the free surface flow. Generally speaking, the fluctuation of the free surface weakened the amplitude response of the PTC cylinder. From the graph, it can be seen that the amplitude in the free surface flow was closer to the experimental data than that in the flow without the free surface. It should be noted that in the experiment conducted in the MRELab, the water channel had a free surface; therefore, in order to eliminate the influence of the free surface, the distance between the cylinder and the free surface was set to 6.5*D*. In the practical experiment, both the flow current and the wave influenced the response of the oscillator. The present numerical simulation method of the combination of the free surface with the dynamic mesh could be a better way to make a more realistic replication of the experiment in the computer.

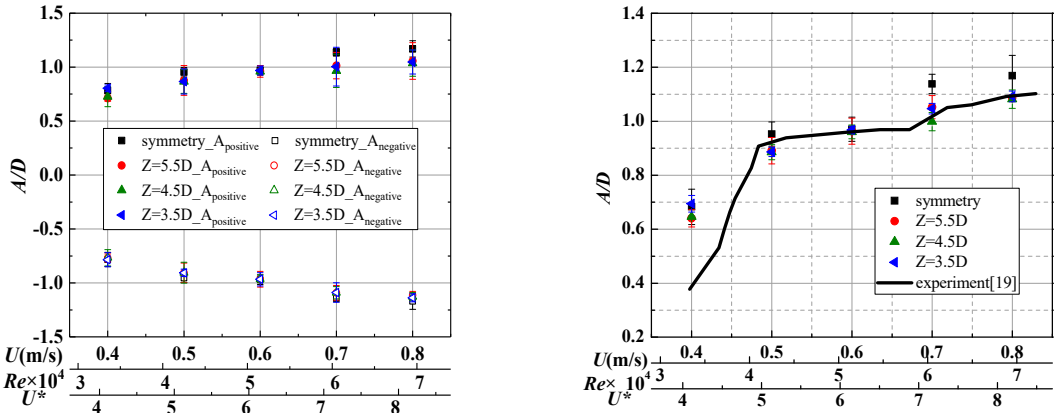

(**a**) Positive and Negative Amplitude Ratios (**b**) Average Amplitude Ratio

Figure 14. The amplitude ratios (*A*/*D*) of the PTC cylinder flow-induced vibration in the free surface flow.

As for the *Re* range, in the present study, the *Re* range was from 3×10^4 to 7×10^4, which belonged to the initial and VIV stage. The PTC could trigger galloping, which corresponded to the *Re* range of 10×10^4 to 13×10^4, and the phenomenon has been widely researched [7–12,14–16,19–21]. In the present simulation with the free surface flow, if the incoming flow velocity was high in the galloping range, the amplitude response of the oscillator was big enough to reach the free surface, which interrupted the calculation. Therefore, the galloping range was not included in the present simulations.

In Figure 15, the flow-induced vibration frequency ratio of the PTC cylinder varied with the Reynolds number in the free surface flow field. With the increase of the Reynolds number, the frequency ratio gradually increased and reached the maximum at $Re = 6.1 \times 10^4$ ($U = 0.7$ m/s), then decreased with the increase of the Reynolds number; when $Z = 4.5D$ and $3.5D$, with the increase of the Reynolds number, the frequency ratio gradually increased and reached the maximum at $Re = 5.3 \times 10^4$ ($U = 0.6$ m/s), and continued to decrease with the increase of the Reynolds number. In the case of the symmetrical flow field, the maximum value was obtained at $Re = 5.3 \times 10^4$ ($U = 0.6$ m/s). It can be seen from the whole figure that the frequency of the free surface flow field was closer to the experimental data than that of the symmetrical flow field.

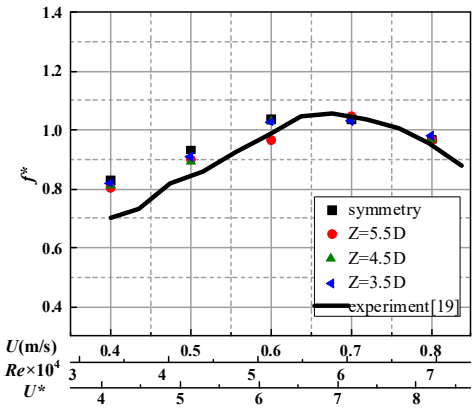

Figure 15. The frequency ratio (f^*) of the PTC cylinder.

3.3.2. Energy Harvesting Characteristics

Figure 16a shows the output power performance of the PTC cylinder in VIVACE when the free surface existed. The energy output power of the PTC cylinder increased with the increase of the Reynolds number at the same free surface height, and the output power could reach the summit when the incoming flow velocity was about 0.7 m/s, which corresponded with the climax of the frequency ratio in Figure 15. The motion of the PTC cylinder caused irregular fluctuations of the free surface. The randomness of the free surface fluctuation made the energy output power of the PTC cylinder change nonlinearly at different free surface heights. There were two main reasons for the difference between the simulated and experimental data: One is that the spring and damping in the experimental system were considered as fixed values, which was different to their own actual non-linearity. The other was that the free surface existed in the experiment, and the immersion depth of the cylinder reached $6.5D$. This can also be seen from the variation trend in the graph, where the higher the free surface height was, the closer the simulation result was to the experimental data.

In Figure 16b, the energy output efficiency of the VIVACE system is shown. With the increase of the Reynolds number, the energy output efficiency of the PTC cylinder decreased for the same free surface height, with the exception of the initial stage from 0.4–0.5m/s, where the exception could be attributed to the fact that in this stage, the flow velocity was small, which made the denominator in Equation (16) small. Under the same Reynolds number, it can be seen that the energy output efficiency in the free surface flow field was greater than that in the symmetrical flow field.

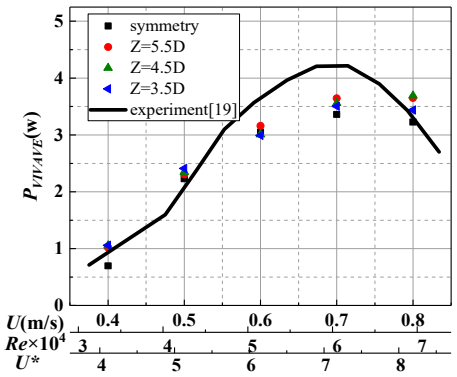

(**a**) Power output of the PTC cylinder in the free surface flow

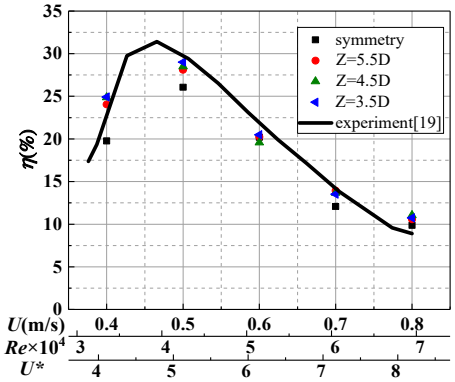

(**b**) Efficiency of the PTC cylinder in the free surface flow

Figure 16. Comparison of the harness power and power conversion efficiency of VIVACE with the PTC cylinder in the free surface flow.

4. Conclusions

In this paper, a numerical simulation technique was adopted to study the hydrodynamic performance of a stationary PTC cylinder and the vortex-induced vibration (VIV) performance of a PTC cylinder in a flow field with a free surface. The simulation technique combining a VOF method with a dynamic mesh was realized, and the influence of the corresponding flow and structure parameters were investigated. The following conclusions can be drawn:

(1) By analyzing the lift and drag time-history curves of flow around the stationary PTC cylinder and the VIV cylinder, it was found that the free surface increased the instability of the shear layer, promoting the formation of a Kármán vortex street, and then reached the periodic steady state quickly, where the stronger the asymmetry, the quicker the stability was achieved. The free surface shortened the starting time of the oscillator, shortened the response time to the incoming flow, and was more easily able to provide dynamic control of the motion of the oscillator in practical engineering applications.

(2) In the flow-induced vibration, due to the moving of the cylinder, the actual incoming flow direction mainly affected the front surface of the cylinder, thus the surface C_p distribution was different from that in the flow around the stationary cylinder, and the upper and lower surfaces of the instantaneous C_p curve intersected.

(3) Within the range of the parameters studied in this paper, the existence of the free surface did not affect the shape of the vortices when the PTC cylinder was stationary. When the PTC cylinder underwent flow-induced vibration, the wake vortices changed faster and new modes appeared faster with the increase of the Reynolds number at the same free surface height. Compared with the symmetrical flow field, the wake region of the free surface flow gradually extended, and the farther the vortex shedding was away from the cylinder, the more energy the multiple vortices had.

(4) In the flow-induced vibration, the existence of the free surface affected the positive amplitude ratio of the PTC cylinder, but had little effect on the negative amplitude ratio. Generally speaking, the fluctuation of the free surface weakened the amplitude response of the PTC cylinder, but compared with the simulation in the uniform asymmetric flow, the simulation results with the free surface were closer to the experimental data.

(5) With the increase of the Reynolds number, the energy output efficiency of the PTC cylinder decreased with the same free surface height, with the exception of the initial stage. Under the same Reynolds number, the energy output efficiency in the free surface flow field was greater than that in the symmetrical flow field.

5. Future Research

In the present study, the main content focused on the response characteristics of the oscillator in the flow field with a free surface, and the fluctuation of the free surface was not studied in depth. The fluctuation of the free surface will affect the vibration of the oscillator to some extent. The relationship between the phase of the free surface fluctuation and the phase of oscillator vibration deserves further study.

Compared to the uniform symmetric incoming flow, the asymmetric flow field with the free surface will have different response characteristics to that of the oscillator. Determining how to use the asymmetry of the flow field or the structure of the vibrator to influence the motion law of the vibrator and then control the movement of the vibrator is also an interesting and useful research direction.

Author Contributions: D.Z. and H.S. conceived of the surface effect on the negative effect of harnessed energy. H.S. developed the Virtual Spring Damping system. With the discussion with Michael Bernitsas, we were encouraged to investigate this phenomenon experimentally and numerically. H.S. carried out the experiment. H.S. and D.Z. wrote the manuscript with support from Bernitsas. D.Z. and H.S. contributed to the design and implementation of the research, to the analysis of the results and to the writing of the manuscript. D.Z. and L.F., H.Y. carried out the CFD of two cylinders FIO, and he wrote Section 3 on the numerical approach. The result and discussions section are written by D.Z., T.L. All authors have read and agreed to the published version of the manuscript.

Funding: This work was supported by the Natural Science Foundation of Shandong Province of China (grant no. ZR2018MEE032), the Natural Science Foundation (no. 51609053), and the Fundamental Research Funds for the Central Universities (grant no. 18CX02131A).

Conflicts of Interest: The authors declare that they have no known competing conflicts of interests or personal relationships that could have appeared to influence the work reported in this paper.

References

1. Feng, C.C. The Measurement of Vortex-Induced Effects on Flow Past Stationary and Oscillating Circular D-Section Cylinders. Ph.D. Thesis, University of British Columbia, Vancouver, BC, Canada, 1986.
2. Sarpkaya, T. A critical review of the intrinsic nature of vortex-induced vibrations. *J. Fluids Struct.* **2004**, *19*, 389–447. [CrossRef]
3. Bearman, P.W. Vortex shedding from oscillating bluff bodies. *Annu. Rev. Fluid Mech.* **2012**, *16*, 195–222. [CrossRef]
4. Williamson, C.H.K.; Govardhan, R. A brief review of recent results in vortex-induced vibrations. *J. Wind Eng. Ind. Aerodyn.* **2008**, *96*, 713–735. [CrossRef]
5. Ali, B.R.; Mohammadmehdi, A. Renewable energy harvesting by vortex-induced motions: Review and benchmarking of technologies. *Renew. Sustain. Energy Rev.* **2016**, *70*, 193–214.
6. Lian, J.; Yan, X.; Liu, F.; Zhang, J.; Ren, Q. Experimental investigation on soft galloping and hard galloping of triangular prisms. *Appl. Sci.* **2017**, *7*, 198. [CrossRef]
7. Bernitsas, M.M.; Raghavan, K.; Ben-Simon, Y.; Garcia, E.M.H. VIVACE (vortex induced vibration aquatic clean energy): A new concept in generation of clean and renewable energy from fluid flow. ASME Transactions November 2008. *J. Offshore Mech. Arct. Eng. (OMAE)* **2006**, *130*, 041101–041115. [CrossRef]
8. Bernitsas, M.M.; Ben-Simon, Y.; Raghavan, K.; Garcia, E.M.H. The VIVACE converter: Model tests at Reynolds numbers around 105. ASME Transactions, February 2009. *J. Offshore Mech. Arct. Eng. (OMAE)* **2006**, *131*, 1–13.
9. Bernitsas, M.M.; Raghavan, K. Fluid Motion Energy Converter, U. S. Patent Trademark Office. U.S. Patent No. 7493759B2, 24 February 2009.
10. Chang, C.C.; Kumar, R.A.; Bernitsas, M.M. VIV and galloping of single circular cylinder with surface roughness at $3 \times 10^4 \leq \mathrm{Re} \leq 1.2 \times 10^5$. *Ocean Eng.* **2011**, *38*, 1713–1732. [CrossRef]
11. Park, H.R.; Kumar, R.A.; Bernitsas, M.M. Enhancement of fluid induced vibration of rigid circular cylinder on springs by localized surface roughness at $3 \times 10^4 \leq \mathrm{Re} \leq 1.2 \times 10^5$. *Ocean Eng.* **2013**, *72*, 403–415. [CrossRef]
12. Park, H.R.; Chang, C.C.; Bernitsas, M.M. Sensitivity to zone covering of the map of passive turbulence control to flow-induced motions for a circular cylinder at 30,000 <Re <120,000. *J. Offshore Mech. Arct. Eng.* **2017**, *139*, 021802.

13. Zhang, X.F.; Liu, F.; Li, Q.; Li, H.; Wang, D.B. Numerical simulation of liquid surface sloshing in IFV heat exchanger of LNG-FSRU regasification module. *Petro Chem. Equip.* **2016**, *19*, 14–19. (In Chinese)
14. Ding, L.; Zhang, L.; Bernitsas, M.M.; Chang, C.-C. Numerical simulation and experimental validation for energy harvesting of single-cylinder VIVACE converter with passive turbulence control. *Renew. Energy* **2016**, *85*, 1246–1259. [CrossRef]
15. Ding, L.; Zhang, L.; Wu, C.; Mao, X.; Jiang, D. Flow induced motion and energy harvesting of bluff bodies with different cross sections. *Energy Convers. Manag.* **2015**, *91*, 416–426. [CrossRef]
16. Ding, L.; Zhang, L.; Kim, E.S.; Bernitas, M.M. URANS vs. experiments of flow induced motions of multiple circular cylinders with passive turbulence control. *J. Fluids Struct.* **2015**, *54*, 612–628. [CrossRef]
17. Karim, M.M.; Prasad, B.; Rahman, N. Numerical simulation of free surface water wave for the flow around NACA 0015 hydrofoil using the volume of fluid (VOF) method. *Ocean Eng.* **2014**, *78*, 89–94. [CrossRef]
18. Mansoorzadeh, S.; Javanmard, E. An investigation of free surface effects on drag and lift coefficients of an autonomous underwater vehicle (AUV) using computational and experimental fluid dynamics methods. *J. Fluids Struct.* **2014**, *51*, 161–171. [CrossRef]
19. Sun, H.; Kim, E.S.; Nowakowski, G.; Mauer, E.; Bernitsas, M.M. Effect of mass-ratio, damping, and stiffness on optimal hydrokinetic energy conversion of a single, rough cylinder in flow induced motions. *Renew. Energy* **2016**, *99*, 936–959. [CrossRef]
20. Zhang, D.H.; Sun, H.; Wang, W.H.; Bernitsas, M.M. Rigid cylinder with asymmetric roughness in flow induced vibrations. *Ocean Eng.* **2018**, *150*, 363–376. [CrossRef]
21. Bernitsas, M.M. Harvesting energy by flow included motions. In *Springer Handbook of Ocean Engineering*; Springer: Cham, Switzerland, 2016; Chapter 47; pp. 1163–1244.
22. ANSYS. *Fluent 19.2 User's Guide*; ANSYS Inc.: Canonsburg, PA, USA, January 2019.
23. Sumer, B.M. Hydrodynamics around cylindrical structures. *Coast. Eng.* **2006**, *33*, 69.